

Ab initio transport coefficients of Ar⁺ ions in Ar for cold plasma jet modelingA. Chicheportiche,^{1,2,*} B. Lepetit,^{3,4} F. X. Gadéa,^{5,6} M. Benhenni,^{1,2} M. Yousfi,^{1,2} and R. Kalus⁷¹Université de Toulouse, UPS, Laboratoire Plasma et Conversion d'Énergie, LAPLACE, Toulouse, France²CNRS, UMR 5213, F-31062 Toulouse, France³Université de Toulouse, UPS, Laboratoire Collisions Agrégats Réactivité, IRSAMC, Toulouse, France⁴CNRS, UMR 5589, F-31062 Toulouse, France⁵Université de Toulouse, UPS, Laboratoire de Chimie et Physique Quantiques, IRSAMC, Toulouse, France⁶CNRS, UMR 5626, F-31062 Toulouse, France⁷Centre of Excellence IT4 Innovations and Department of Applied Mathematics, VSB, Technical University of Ostrava, 17. listopadu 15/2172, 708 33 Ostrava, Poruba, Czech Republic

(Received 29 January 2014; revised manuscript received 7 March 2014; published 10 June 2014)

Collision cross sections and transport coefficients are calculated for Ar⁺ ions, in the ground state ²P_{3/2} and in the metastable state ²P_{1/2}, colliding with their parent gas. Differential and integral collision cross sections are obtained using a numerical integration of the nuclear Schrödinger equation for several published interaction potentials. The Cohen-Schneider semi-empirical model is used for the inclusion of the spin-orbit interaction. The corresponding differential collision cross sections are then used in an optimized Monte Carlo code to calculate the ion transport coefficients for each initial ion state over a wide range of reduced electric field. Ion swarm data results are then compared with available experimental data for different proportions of ions in each state. This allows us to identify the most reliable interaction potential which reproduces ion transport coefficients falling within the experimental error bars. Such ion transport data will be used in electrohydrodynamic and chemical kinetic models of the low temperature plasma jet to quantify and to tune the active species production for a better use in biomedical applications.

DOI: [10.1103/PhysRevE.89.063102](https://doi.org/10.1103/PhysRevE.89.063102)

PACS number(s): 52.20.Hv, 51.50.+v, 52.25.Fi

I. INTRODUCTION

In low temperature plasma generated in noble gases, ion swarm data are needed to optimize the features of many devices devoted for instance to biomedical applications [1]. More particularly, they can be used in electrohydrodynamic and chemical models of the low temperature plasma jets, to quantify and to tune the production of active species for a better use in the medical field for antitumor treatment, wound healing, blood coagulation, and others; Ref. [2] and the references given therein provide more information on this topic. For instance, the interaction of low temperature plasmas with cancerous cells has been studied for several years. It was clearly found in *in vitro* studies that the plasma induced cancer cell apoptosis, and that a size reduction of microtumor xenografted occurs in the case of animal or murine experimentation. However, the plasma species responsible for these effects are not yet clearly identified and require further research (see, e.g., Refs. [1] and [2]).

Moreover, to tune such plasma sources to each specific biomedical application, it is very important to better understand the mechanisms of formation and propagation of observed fast plasma bullets or ionization waves in the plasma jet devices. Electrohydrodynamic and chemical plasma models are in complement to experimental measurements and are useful tools to study the physical phenomena and to accurately quantify the generated active species [3]. However, the use of such models requires a good knowledge of ion swarm input data such as reduced mobility, diffusion coefficients, and reaction rates.

Many low temperature plasma devices use a helium carrier due to the relatively low voltage required to ignite an electrical discharge [1]. The transport data of He⁺ and He₂⁺ ions have been already studied in detail elsewhere [4,5]. However, in order to generate plasma jets with different active species for different potential biomedical applications, it is interesting to investigate other carrier gases such as argon. Moreover, this allows one to anticipate the future shortage of helium worldwide production and also to use a gas which is more easily available and cheaper than helium. Argon has been already used to generate low temperature plasma jets in the biomedical field [6,7]. For instance, a plasma jet using argon carrier gas at low flow velocity (a few m/s) can be initiated in a glass tube (about 10 mm diameter) involving a concentric tungsten wire having small diameter (see, e.g., [7]). Such a thin electrode (e.g., 0.6 mm diameter) that is powered with a pulsed high voltage (a few kV and kHz), generates a high electric field [around 100 Td (1 Td = 10⁻¹⁷ V cm²)] around the tip of the wire inside the glass tube, which initiates the plasma jet propagation along the tube axis. The active plasma species needed for biomedical applications (radicals, long living excited species, ions, UV photons, etc.) are produced in open air and are strongly dependent on the magnitude of the space-charge electric field that propagates the plasma jet outside the tube. It is noteworthy that the magnitude of the space-charge electric field is totally controlled by the transport of argon ions when using argon as a carrier gas. This means that the kinetics of argon ions can also play a significant role in the formation of the active species [8]. Therefore, a good knowledge of ion transport coefficients is absolutely necessary for an accurate determination of the space-charge electric field (i.e., the electric field self-generated by ionization waves) and to quantify the produced active species.

*chicheportiche@laplace.univ-tlse.fr

Atomic argon ions can be found in the plasma jet in two different fine structure states. A fraction of Ar^+ is in the ground state level labeled $^2P_{3/2}$ where $J = 3/2$ is the total (orbital + spin) angular momentum of the ion. This corresponds to two possible absolute values $\Omega = (1/2, 3/2)$ for the projection of this total angular momentum on a given axis. Another fraction is in the metastable state $^2P_{1/2}$ where $J = 1/2$ and includes ions with $\Omega = 1/2$ only. In weakly ionized gases, corresponding to the low temperature plasma jet under the action of an external electric field, the ion transport coefficients are closely related to the ion-neutral interaction potential curves and can be derived from the corresponding collision cross sections. The purpose of this work is to compute accurate transport coefficients for the ions in both the ground state $^2P_{3/2}$ and the metastable state $^2P_{1/2}$ using an optimized Monte Carlo code [9]. These transport coefficients are obtained using the differential collision cross sections calculated for several *ab initio* interaction potentials given in the literature. For the diatomic argon ion, the spin-orbit (SO) coupling is important and we have taken it into account following the Cohen-Schneider *atoms-in-molecules* model [10] where the SO atomic coupling scheme is extended to the molecule. The main effect is a splitting of the molecular potential curves at large distances consistent with the atomic fine structure splitting. Therefore, we have performed calculations of transport coefficients for ions in the ground and metastable states. By comparison of ion transport coefficients with available experimental data [11–14], we can assess the accuracy of the diatomic potentials that were used.

Following this introduction, Sec. II is devoted to the description of the interaction potentials of the Ar^+/Ar interaction system without the inclusion of the spin-orbit couplings [15–18]. The Cohen-Schneider semiempirical model is then briefly described for the inclusion of the spin-orbit interaction [10]. In Sec. III the close coupling quantum method [19,20] is used to calculate the collision cross sections for the possible electronic transitions of Ar^+ ions colliding with Ar. Since we are interested in the calculation of ion transport coefficient at room temperature (300 K corresponding to a mean gas energy of 0.04 eV), collision cross sections for energies below 1 meV are not considered here. The collision cross section for ions in the ground $^2P_{3/2}$ state and the metastable $^2P_{1/2}$ state are then presented over a limited center-of-mass energy range varying from 1 meV to 12 eV. In Sec. IV a short description of the Monte Carlo method is given followed by a comparison of the transport coefficients obtained at $T = 300$ K by using different interaction potentials, for both electronic states of Ar^+ ($^2P_{3/2}$ and $^2P_{1/2}$), and over a wide range of reduced electric field E/N (E is the electric field and N the gas density) varying from 1 to 1500 Td. Moreover, the effect of the spin-orbit couplings on the mobility will also be tested in this study. Since experimental data contain an unknown proportion of Ar^+ ions in the metastable state, a comparative analysis of ion transport coefficients calculated for different ions proportions in the metastable state is done to provide information on the accuracy of the molecular potentials and to decide between different experimental data. Finally, we draw some conclusions in Sec. V.

II. INTERACTION POTENTIALS

The first excited neutral and ionic Ar states are 11.6 eV [$\text{Ar}: 3s^23p^5(^2P_{3/2})4s$] and 15.8 eV ($\text{Ar}^+: 3p^5(^2P_{3/2})$) [21] above the ground state of the neutral atom, respectively, and the first excited state of Ar_2^+ is asymptotically about 12 eV above the ground state of the ionic dimer. Therefore, for the low Ar^+/Ar collision energies considered here, one needs to take into account only the states \sum_u^+ , \prod_g , \prod_u , and \sum_g^+ which dissociate to the lowest limit of $\text{Ar}^+ + \text{Ar}$. In order to get accurate ion transport coefficient results, several Ar_2^+ interaction potentials available from the literature without the inclusion of the spin-orbit (SO) interaction have been considered in this study. The SO couplings are then taken into account using the Cohen-Schneider semiempirical model [10].

Barata *et al.* [15] give an analytical form for the four lowest electronic states of Ar_2^+ depending on several parameters adjusted in order to reproduce experimental high-resolution photoelectron spectroscopy data, dissociation energies D_e , and equilibrium internuclear distances r_e , reported by Wüest and Merkt [22]. Whitaker *et al.* [16] determined *ab initio* Born-Oppenheimer (BO) potentials over a grid of points using a Gaussian basis set and a nonrelativistic single reference configuration interaction (CI). Gadéa and Paidarová [17] and Ha *et al.* [18] also used nonrelativistic CI *ab initio* calculations with large basis sets to determine the potential energy curves of Ar_2^+ . Since the literature potentials are mostly reported as tables of points [16–18], a cubic spline interpolation has been employed here for the intermediate internuclear distance range. A couple of points were added in the intermediate attractive region by using the following function, in order to remove oscillations caused by the spline interpolation:

$$V^{\text{att}}(r) = -\frac{\alpha_1}{2r^4} - \frac{C_6}{r^6} - \frac{C_8}{r^8} + D, \quad (2.1)$$

where $V^{\text{att}}(r)$ is the attractive interaction potential, r is the internuclear distance, and α_1 , C_6 , C_8 , and D are constants to be determined in order that $V^{\text{att}}(r)$ fits best the *ab initio* points given in the intermediate attractive region. Outside this range, potential curves were extrapolated at long range by the standard attractive polarization potential:

$$V^l(r) = -\frac{\alpha}{2r^4} + D, \quad (2.2)$$

where $V^l(r)$ is the long-distance potential energy and $\alpha = 10.891$ a.u. is the polarizability of argon. For short internuclear distances, the interaction potential curves were extrapolated using the following relation:

$$V^s(r) = Ae^{-Br} + C, \quad (2.3)$$

where $V^s(r)$ is the short-distance potential and A , B , and C are three constants calculated in order to fit three shortest distance *ab initio* discrete points. However, the three shortest distance points given by Whitaker *et al.* [16] and Gadéa and Paidarová [17] for \sum_u^+ and \prod_g are too close to the potential well to use the relation (2.3) for a repulsive extrapolation. Therefore, an analytic exponential form was used to fit the difference

TABLE I. Parameters of Eqs. (2.1)–(2.3) in a.u. used for the interpolation and extrapolation of Whitaker *et al.*'s [16], Gadéa and Paidarová's [17], and Ha *et al.*'s [18] Ar_2^+ potential curves without inclusion of the spin-orbit interaction.

Ref. of potentials	State	α_1	C_6	C_8	A	B	C	D
Whitaker <i>et al.</i> [16]	Σ_u^+	14.19	3.08×10^3	4.72×10^5	571.3	2.422	-6.12×10^{-2}	2.45×10^{-8}
	Π_g	9.45	114.34	3.01×10^4	163.5	1.864	-1.31×10^{-2}	6.45×10^{-8}
	Π_u	9.66	285.20	-2.84×10^4	112.2	1.643	-7.88×10^{-3}	6.45×10^{-8}
	Σ_g^+	11.04	1592.4	-3.04×10^5	46.94	1.355	-8.25×10^{-3}	2.45×10^{-8}
Gadéa and Paidarová [17]	Σ_u^+	–	–	–	768.4	2.527	–41.5809	–41.521
	Π_g	–	–	–	184.0	1.910	–41.5366	–41.521
	Π_u	–	–	–	152.6	1.748	–41.5210	–41.521
	Σ_g^+	–	–	–	43.08	1.334	–41.5209	–41.521
Ha <i>et al.</i> [18]	Σ_u^+	11.55	4.90×10^4	-4.16×10^7	328.4	2.272	-9.32×10^{-1}	–0.859 2018
	Π_g	12.96	1.65×10^4	-1.86×10^7	99.16	1.717	-8.91×10^{-1}	–0.859 2018
	Π_u	14.27	9.52×10^3	-1.45×10^7	49.13	1.374	-9.23×10^{-1}	–0.859 2018
	Σ_g^+	11.26	5.00×10^4	-4.20×10^7	51.45	1.404	-8.29×10^{-1}	–0.859 2018

between the potential curves of Whitaker *et al.* or Gadéa and Paidarová and Ha in this region. This allowed us to obtain energy points for Gadéa and Paidarová and Whitaker *et al.* at shorter distances than the ones given in original papers and to use Eq. (2.3) to extrapolate the potentials at short internuclear distances. The parameters α_1 , C_6 , C_8 , and D used in Eqs. (2.1)–(2.3) for interpolation at intermediate range and A , B , C parameters for the extrapolation at short distance of the *ab initio* electronic states Σ_u^+ , Π_g , Π_u , and Σ_g^+ of Refs. [16–18] are listed in Table I. The value of α_1 is close to the polarizability α of argon while the C_6 and C_8 parameters are much more dependent on the *ab initio* calculation and act as corrective terms. It should be however emphasized that in all cases, extrapolation at long distance follows only Eq. (2.2). The parameter D depends primarily on the kind of *ab initio* calculation, i.e., if pseudopotentials are used or not for example. Figure 1 shows the four lowest electronic states given by Ha *et al.* [18] for the Ar^+/Ar interaction system. The typical behavior of these potentials can be understood on the basis of simple mono-electronic pictures. For the σ or π bonds, which present respectively an axial or lateral overlap, there

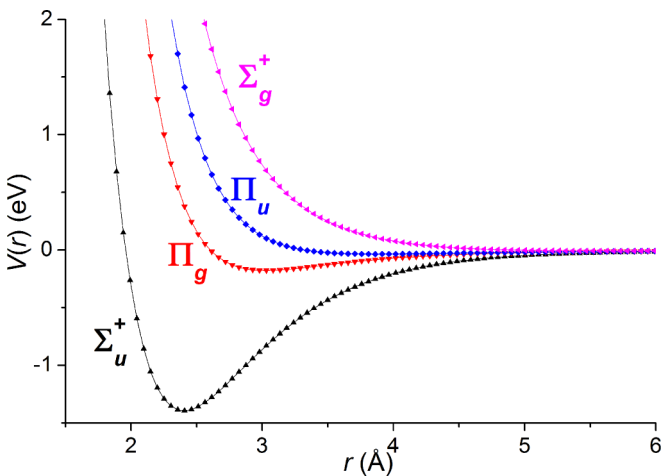


FIG. 1. (Color online) Interaction potential curves for the Ar^+/Ar interaction system in the four lowest electronic states Σ_u^+ , Π_g , Π_u , and Σ_g^+ without inclusion of the spin-orbit interaction.

is a strong attractive interaction when an electron is removed from a strongly antibonding orbital (respectively, σ_u or π_g) and a strong repulsive interaction when it is removed from a bonding orbital (respectively, σ_g or π_u).

At intermediate and short interatomic distances, the spin-orbit coupling is small compared to the electrostatic interactions and the Ar_2^+ dimer presents four well separated curves. At the long-distance range, the molecular interactions vanish and as the four curves approach degeneracy and converge to the asymptotic limit, the spin-orbit coupling becomes the dominant interaction. In order to obtain potential curves with the inclusion of the spin-orbit interaction, the Cohen-Schneider model [10] has been used. This model introduces a mixing between the different adiabatic interaction potential curves Σ and Π (without inclusion of the spin-orbit) which have the same Ω and g/u symmetry as presented in the matrix given in Table II. Diagonalizing this matrix for each value of internuclear distance r leads to six adiabatic interaction potential curves if the spin-orbit interaction is considered. These states are labeled, in ascending order of energy, $I(1/2)_u$, $I(3/2)_g$, $I(1/2)_g$, $I(3/2)_u$, $II(1/2)_u$, and $II(1/2)_g$, where Ω is given in parentheses and the symmetry label g/u is in the subscript. I or II corresponds, respectively, to $J = 3/2$ and $J = 1/2$ asymptotically. Adiabatic interaction potential curves including the spin-orbit interaction are displayed in Fig. 2. The asymptotic energy difference ΔE_p between the states $\text{Ar}^+(^2P_{3/2}) + \text{Ar}(^1S)$ and $\text{Ar}^+(^2P_{1/2}) + \text{Ar}(^1S)$ is related to the fine structure atomic parameter $a = 0.11833$ eV [21]:

$$\Delta E_p = \frac{3}{2}a = 0.1775 \text{ eV.}$$

TABLE II. Electronic Hamiltonian according to the Cohen-Schneider semiempirical model [10] for each symmetry g/u .

	$\Sigma_{1/2}^+$	$\Pi_{1/2}$	$\Pi_{3/2}$
$\Sigma_{1/2}^+$	$E_{\Sigma_{g,u}^+}$	$-a/\sqrt{2}$	0
$\Pi_{1/2}$	$-a/\sqrt{2}$	$E_{\Pi_{g,u}} + a/2$	0
$\Pi_{3/2}$	0	0	$E_{\Pi_{g,u}} - a/2$

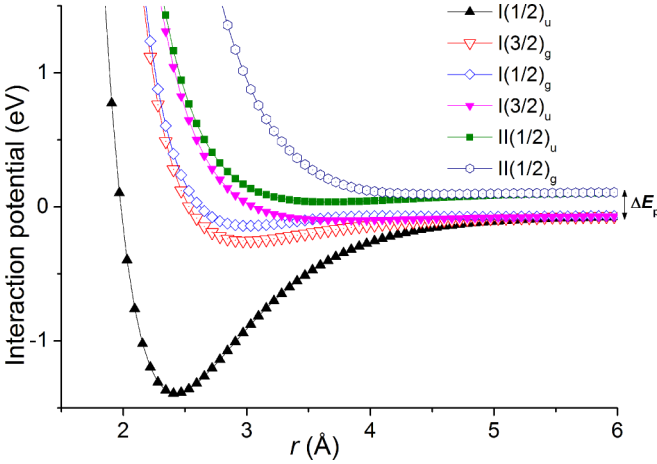


FIG. 2. (Color online) Interaction potential curves with inclusion of the spin-orbit interaction for the six lowest electronic states of Ar_2^+ .

Therefore, inelastic spin change processes cannot take place for collision energies below about 0.18 eV and have thus no effect on the ion transport coefficients at low electric fields.

Absolute deviations in meV between Ha *et al.*'s potential curves with the inclusion of the SO interaction and other potentials are displayed in Fig. 3. Ha *et al.*'s potentials have been taken as a reference since they are the most recent ones. We can see from this figure that the deviations increase for all the potential curves in the short-range repulsive part. Moreover, at intermediate and large interatomic distances, the interaction potential curves $\text{I}(3/2)_u$ and $\text{I}(3/2)_g$ of Barata *et al.* and Gadéa and Páidarová are rather close to each other. We can thus expect that for $\Omega = 3/2$, collision cross sections calculated from Barata *et al.* and Gadéa and Páidarová's potentials would be similar at low collision energies.

III. COLLISION CROSS SECTIONS

We consider here differential, integral, and momentum transfer collision cross sections. A description of the formalism used to compute cross sections has been already given elsewhere [19,20]. In short, assuming that argon nuclei are distinguishable and using partial wave expansion with angular momentum l , the scattering amplitude at collision energy ε in angle θ for a particle coming from the initial internal state or channel i to the final one j is given by

$$f_{ij}(\varepsilon, \theta) = -\frac{1}{2i(k_i k_j)^{1/2}} \sum_l (2l+1) T_{ij}^l(\varepsilon) P_l(\cos \theta), \quad (3.1)$$

where k_i and k_j are initial and final wave vectors, $T_{ij}^l(\varepsilon)$ is a transition matrix element, and $P_l(\cos \theta)$ are the Legendre polynomials of order l . The transition matrix elements are obtained after numerical integration of the coupled differential equations resulting from the expansion of the total wave function of the system on the molecular state basis associated with the potentials described in Sec. II. This molecular wave function method corresponds to a numerical integration of the nuclear Schrödinger equation without semiclassical approximation which is efficient for the rather low collision

energies considered here (for more details, see Sec. M.5 in [20]). Integral $\sigma_0^{ij}(\varepsilon)$ and momentum transfer $\sigma_1^{ij}(\varepsilon)$ cross sections from initial channel i to final one j are obtained by integration over solid angle χ :

$$\sigma_0^{ij}(\varepsilon) = \frac{k_j}{k_i} \int d\chi |f_{ij}(\varepsilon, \theta)|^2 \quad (d\chi = 2\pi \sin \theta d\theta), \quad (3.2)$$

$$\sigma_1^{ij}(\varepsilon) = \frac{k_j}{k_i} \int d\chi (1 - \cos \theta) |f_{ij}(\varepsilon, \theta)|^2, \quad (3.3)$$

so that

$$\sigma_0^{ij}(\varepsilon) = \frac{\pi}{k_i^2} \sum_l (2l+1) |T_{ij}^l(\varepsilon)|^2, \quad (3.4)$$

$$\sigma_1^{ij}(\varepsilon) = \frac{\pi}{k_i^2} \sum_l \{ (2l+1) |T_{ij}^l(\varepsilon)|^2 - 2(l+1) \times \text{Re}[T_{ij}^l(\varepsilon)^* T_{ij}^{l+1}(\varepsilon)] \}, \quad (3.5)$$

Re referring to the real part of the product of transition matrix elements.

We first do not take into account the fact that the two interacting Ar atoms are identical. As spin-orbit couplings exist only between states which have the same Ω , the latter is conserved during the collision, whereas J can be modified. We note here $(J_i, \Omega \rightarrow J_f, \Omega)^{\text{NCT}}$ (NCT: no charge transfer) the transition corresponding to the process

$$\text{Ar}^+(J_i, \Omega) + \text{Ar} \rightarrow \text{Ar}^+(J_f, \Omega) + \text{Ar}$$

and $(J_i, \Omega \rightarrow J_f, \Omega)^{\text{CT}}$ (CT: charge transfer) the transition for

$$\text{Ar}^+(J_i, \Omega) + \text{Ar} \rightarrow \text{Ar} + \text{Ar}^+(J_f, \Omega).$$

The global problem involving six coupled potentials (cf. Table II) can be split into two separate simpler ones for each subspace $\Omega = 3/2$ and $\Omega = 1/2$. For $\Omega = 3/2$, the calculation involves only the two potential curves $\text{I}(3/2)_{u,g}$ with the same asymptotical energy, corresponding to the two possible localizations of the electron. At this step, these two potential curves are assumed coupled since colliding partners are not identical. In this case, only the elastic $(3/2, 3/2 \rightarrow 3/2, 3/2)^{\text{NCT}}$ and charge transfer $(3/2, 3/2 \rightarrow 3/2, 3/2)^{\text{CT}}$ transitions (without spin change) can take place. For the subspace $\Omega = 1/2$, the four coupled potentials curves $\text{I}(1/2)_{u,g}$ and $\text{II}(1/2)_{u,g}$ are involved. The asymptotical limits of I and II states are separated by an energy ΔE_p (cf. Sec. II). Then, in this case four NCT and CT processes can take place: three transitions are without a threshold in kinetic energy, $(3/2, 1/2 \rightarrow 3/2, 1/2)^{\text{NCT,CT}}$, $(1/2, 1/2 \rightarrow 1/2, 1/2)^{\text{NCT,CT}}$, and $(1/2, 1/2 \rightarrow 3/2, 1/2)^{\text{NCT,CT}}$; while one $(3/2, 1/2 \rightarrow 1/2, 1/2)^{\text{NCT,CT}}$ has a kinetic energy threshold of ΔE_p . Figure 4 displays schematically the possible ion transitions, where the charge is initially localized on one of the two argon atoms and when the two colliding particles are supposed distinguishable.

We now take into account the fact that the colliding partners are identical ^{40}Ar nuclei (99.6003%). This allows g/u separation and reduces the 2×2 problem (for $\Omega = 3/2$) into two single ones. Similar separation can be done for subspace $\Omega = 1/2$ and the 4×4 problem is reduced into two 2×2 simple ones. Moreover, the resonant charge transfer processes $[\text{Ar}^+(J_i, \Omega) + \text{Ar} \rightarrow \text{Ar} + \text{Ar}^+(J_f, \Omega)]$ occurring in direction $(\pi - \theta)$ are

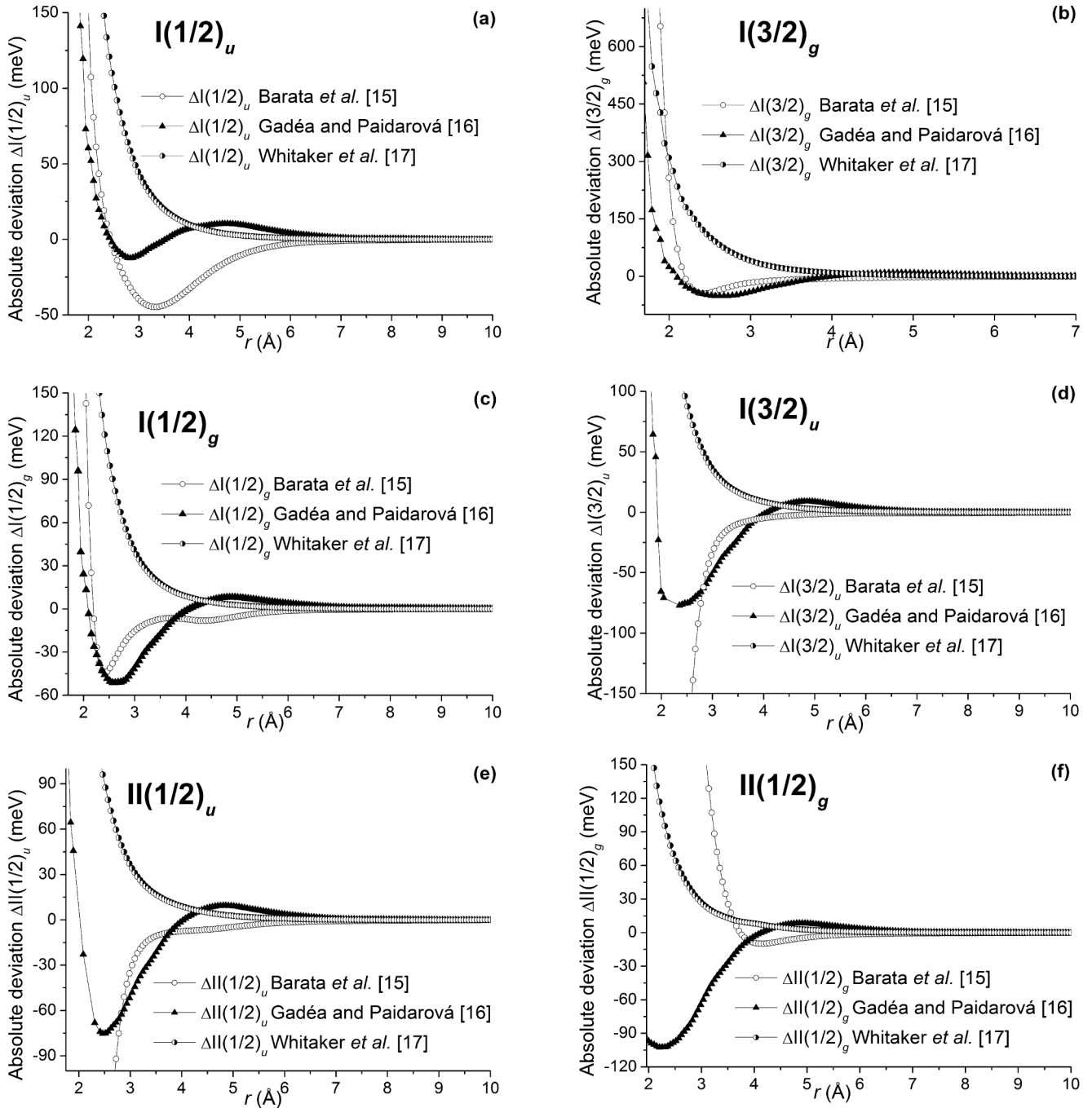


FIG. 3. Absolute deviation between the potential curves (a) $I(1/2)_u$, (b) $I(3/2)_g$, (c) $I(1/2)_g$, (d) $I(3/2)_u$, (e) $II(1/2)_u$, and (f) $II(1/2)_g$ given by Refs. [15–17] and those given by Ha *et al.* [18].

not distinguishable from the no charge transfer ones $[Ar^+(J_i, \Omega) + Ar \rightarrow Ar^+(J_f, \Omega) + Ar]$ occurring in θ direction. As a result, symmetrized scattering amplitude $f_{\text{sym}}(\varepsilon, \theta)$ must be defined as a linear combination of NCT and CT for each spin state as follows:

$$f_{\text{sym}}(\varepsilon, \theta) = f_{\text{NCT}}(\varepsilon, \theta) + f_{\text{CT}}(\varepsilon, \pi - \theta). \quad (3.6)$$

This leads to one symmetrized integral and momentum transfer collision cross section $^s\sigma_{\sigma(J_i, \Omega \rightarrow J_f, \Omega)}(\varepsilon)$ for each possible transition $(J_i, \Omega \rightarrow J_f, \Omega)$. We then have one symmetrized

integral and momentum collision cross section for $\Omega = 3/2$ and four for $\Omega = 1/2$. Transition matrices were obtained by a simple numerical integration from r_{min} to r_{max} over the corresponding potential using the De Vogelaere algorithm [23]. We typically used $r_{\text{min}} = 1.3 \text{ \AA}$ and r_{max} varying between 25 and 100 \AA and the integration was performed with 20 points per wavelength.

To calculate the ion transport coefficients, the symmetrized differential collision cross sections and Eq. (3.2) were used. Indeed, the quantum calculation provides us finite differential

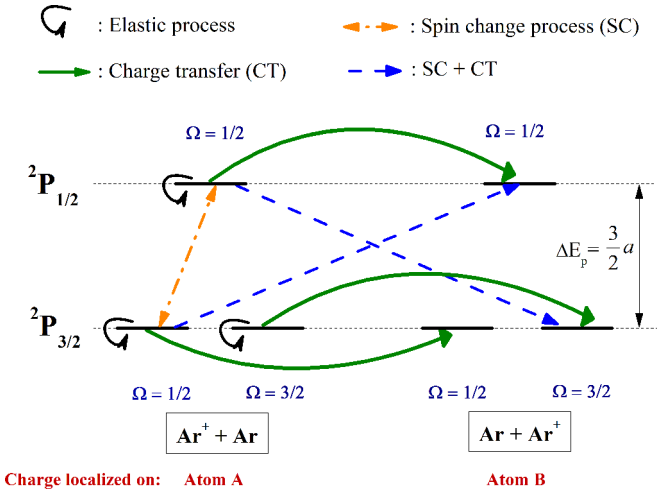


FIG. 4. (Color online) Schematic representation of the possible ion transitions induced by a collision between two argon atoms A and B and when the charge is initially localized on atom A.

cross sections (contrary to classical mechanics calculation) which can be used for an accurate Monte Carlo calculation. However, if only finite momentum transfer collision cross sections are available, it has previously been shown [4] that their use in Monte Carlo simulation considering an isotropic scattering, allows us to obtain the ion transport coefficients with a much shorter computation time and maximal relative deviation of $\pm 2\%$ from the exact results. This method remains valid even in a case of strong anisotropy [4]. Comparison between mobilities of Ar^+ ions in Ar obtained with the two methods will be done in Sec. IV. For inelastic processes, this approximate method is an extension of the usual one based on the momentum transfer collision cross section in the elastic case. Figure 5 displays an example of the symmetrized $(3/2, 3/2 \rightarrow 3/2, 3/2)$ differential cross sections obtained from Ha *et al.*'s $I(3/2)_{u,g}$ interaction potential curves at two

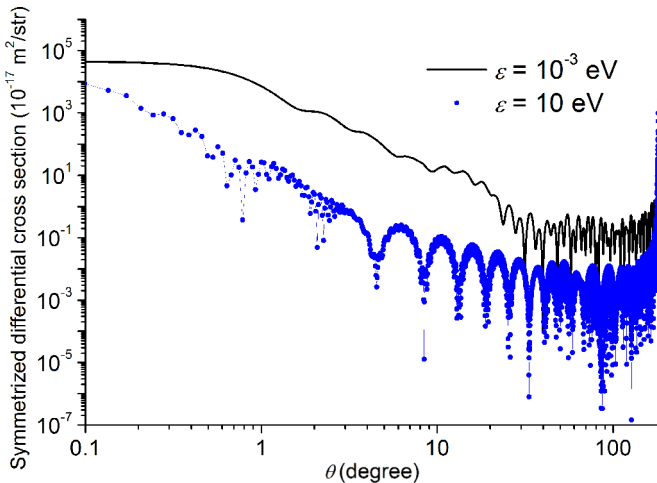


FIG. 5. (Color online) Differential collision cross sections as a function of the ion scattering angle θ in degree calculated from the interaction potential curves of Ha *et al.* [18] for $\varepsilon = 10^{-3}$ eV and $\varepsilon = 10$ eV.

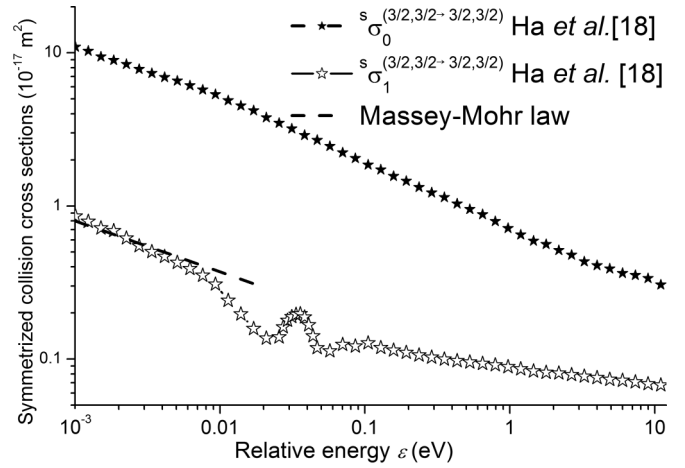


FIG. 6. Symmetrized integral (filled stars) and momentum transfer (empty stars) collision cross sections for the Ha *et al.*'s [18] interaction potentials and for collision energies varying from 1 meV to 12 eV. The Massey-Mohr law at low energy is shown as a dashed line.

different collision energies ε . A complex variation of the differential cross sections with a strong anisotropy in the forward and backward directions is clearly seen. By comparing the corresponding integral and momentum transfer collision cross sections (cf. Fig. 6), we see that the momentum transfer collision cross section ${}^s\sigma_1$ is smaller than the integral collision cross section ${}^s\sigma_0$. This can be easily understood since the large contributions at small and large scattering angles, i.e., $\theta \rightarrow 0^\circ$ and $\theta \rightarrow 180^\circ$, are eliminated by weighting the differential collision cross section by $(1 - \cos \theta)$. This remains valid for all collision energies ε . Similarly to Ref. [4], we interpret the observed oscillations on the collision cross sections as a result of glory scattering [19]. If these oscillations are smoothed out, the collision cross sections decrease according to the Massey and Mohr law, which in the present ion-atom case (long range attractive potential $1/r^4$) is a $\varepsilon^{-1/3}$ power law in the low energy range (cf. Eq. (185) on p. 172 in Ref. [24]). It is shown by the dashed line on the log-log plot of Fig. 6. The slower linear decrease of the cross sections at high energies in Figs. 6–10 is due to the repulsive part of the potential. In the intermediate energy range, the interference of this direct contribution with forward scattering glory contribution provides the oscillations observed in Figs. 6–10. Their amplitudes however are smaller than in the helium case due to the higher masses of the present collision partners (cf. Eq. (191) on p. 175 in Ref. [24]).

The symmetrized momentum transfer ${}^s\sigma_1^{(J_i, \Omega \rightarrow J_f, \Omega)}(\varepsilon)$ collision cross sections, calculated for the potentials mentioned above in Sec. II, are displayed in Fig. 7 for subspace $\Omega = 3/2$ and in Fig. 8 for subspace $\Omega = 1/2$. As shown in Fig. 7, the collision cross sections ${}^s\sigma_1^{(3/2, 3/2 \rightarrow 3/2, 3/2)}(\varepsilon)$ obtained from Barata *et al.*'s [15] and Gadéa and Paidarová's [17] potentials are close to each other at low collision energies. This behavior results from the fact that both potentials are similar at intermediate and large interatomic distances. However, at high energies ε , Barata *et al.*'s potentials give collision cross sections quite different from the ones calculated using the other potentials [16–18]. Indeed, the cross section obtained

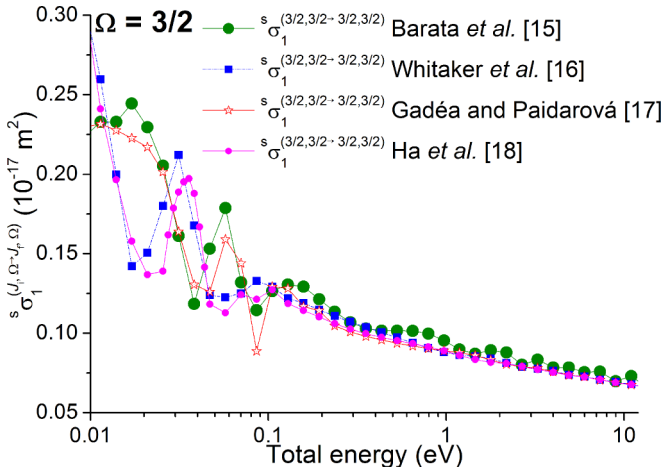


FIG. 7. (Color online) Symmetrized momentum transfer collision cross sections as function of collision energy obtained from the several interaction potential curves [15–18] with the inclusion of the spin-orbit interaction for subspace $\Omega = 3/2$.

for Barata *et al.*'s potentials is higher than the other ones at high collision energies and would lead to lower ion transport coefficients. Figures 8(a) and 8(b) also show that the collision cross sections obtained from Barata *et al.* for subspace

$\Omega = 1/2$ are higher at high collision energies. They would then lead to lower ion transport coefficients at high reduced electric fields compared to the ones calculated for the other potentials. Moreover, Fig. 8(c) shows that the inelastic spin change transition $(3/2, 1/2 \rightarrow 1/2, 1/2)$ would not play an important role in the ion transport coefficient calculations, since the corresponding collision cross sections are negligible. Indeed, this collision cross section is at least about two orders of magnitude smaller than the other ones for subspace $\Omega = 3/2$ and $\Omega = 1/2$.

By applying the microreversibility principle,

$$k_i^2 \sigma^{(i \rightarrow j)}(\epsilon) = k_j^2 \sigma^{(j \rightarrow i)}(\epsilon), \quad (3.7)$$

where i : $(3/2, 1/2)$ and j : $(1/2, 1/2)$, we can obtain the collision cross section for the inelastic spin change transition $(j \rightarrow i)$ from the $(i \rightarrow j)$ cross section. In particular, at large kinetic energies with respect to the energy release of the process ($\Delta E_p = 0.18$ eV), $k_j^2 \approx k_i^2$ and both collision cross sections are close. However, at low energies, $k_j^2 \ll k_i^2$ so that $\sigma^{(j \rightarrow i)}(\epsilon) \gg \sigma^{(i \rightarrow j)}(\epsilon)$. Thus, because both $(3/2, 1/2 \rightarrow 1/2, 1/2)$ and $(1/2, 1/2 \rightarrow 3/2, 1/2)$ collision cross sections are small in a wide energy range, the adiabatic basis, i.e., the uncoupled $I(1/2)_{u,g}$ and $II(1/2)_{u,g}$ interaction potential curves can be used for the cross section and ion transport coefficients calculation. This is what was done in the collision cross section

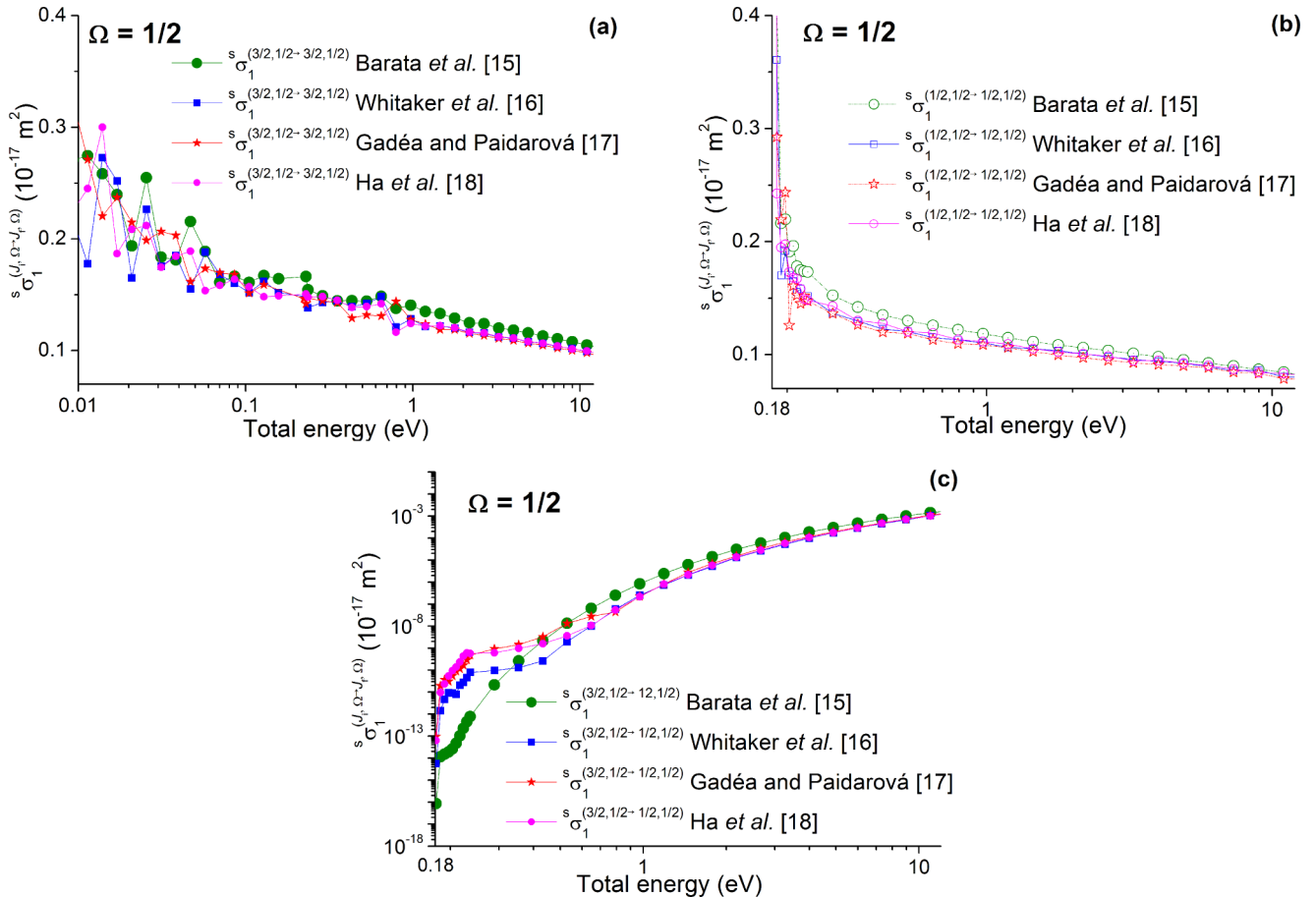


FIG. 8. (Color online) Symmetrized momentum transfer collision cross sections as function of collision energy for the transitions (a) $(3/2, 1/2 \rightarrow 3/2, 1/2)$, (b) $(1/2, 1/2 \rightarrow 1/2, 1/2)$, and (c) $(3/2, 1/2 \rightarrow 1/2, 1/2)$ obtained from the several interaction potential curves [15–18] with the inclusion of the spin-orbit interaction for subspace $\Omega = 1/2$.

calculation of Ref. [15] and the results obtained therein are close to ours within $\pm 5\%$.

Finally, the needed collision cross sections (differential, integral and momentum transfer) for the ion transport coefficients calculation are obtained for each internal energy level of Ar^+ , $^2P_{3/2}$ and $^2P_{1/2}$, by summing over the final states and averaging over the initial ones as follows:

$$Q(^2P_{3/2}) = \frac{1}{2} [s\sigma^{(3/2,3/2 \rightarrow 3/2,3/2)} + s\sigma^{(3/2,1/2 \rightarrow 3/2,1/2)} + s\sigma^{(3/2,1/2 \rightarrow 1/2,1/2)}], \quad (3.8)$$

$$Q(^2P_{1/2}) = s\sigma^{(1/2,1/2 \rightarrow 1/2,1/2)} + s\sigma^{(1/2,1/2 \rightarrow 3/2,1/2)}. \quad (3.9)$$

Figure 9 displays the symmetrized and averaged momentum transfer collision cross sections Q_1 , calculated for the considered interaction potentials [15–18] for the Ar^+/Ar interaction system and for the $^2P_{3/2}$ state of Ar^+ . The momentum transfer collision cross section obtained by Phelps [25] using a ‘‘Langevin’’ polarization scattering method is also plotted for comparison. The data by Phelps show a good agreement with our cross section obtained from Barata *et al.*’s interaction potential curves [15]. However, Phelps [25] does not give cross section values for energies below 0.1 eV (cf. Fig. 9), which does not allow us to calculate the ion transport coefficients for the ions in the ground state $^2P_{3/2}$ at low electric fields. In Fig. 9 we can further notice that the collision cross sections obtained for the potentials given by Whitaker *et al.* [16], Gad ea and Paidarova [17], and Ha *et al.* [18] are very similar to each other at high collision energies. The corresponding ion transport coefficients will be then very close at high electric fields. In the intermediate region, it is noteworthy that the potentials by Whitaker *et al.* and Gad ea and Paidarova present quite similar collision cross sections. We can then expect that the corresponding ion transport coefficients calculated from these two potentials will be close at low electric fields.

Figure 10 shows the collision cross sections obtained for the $^2P_{1/2}$ state of Ar^+ ion and for kinetic energies varying from 0.01 to about 12 eV. A global overview on these collision cross sections can predict that the ion transport coefficients

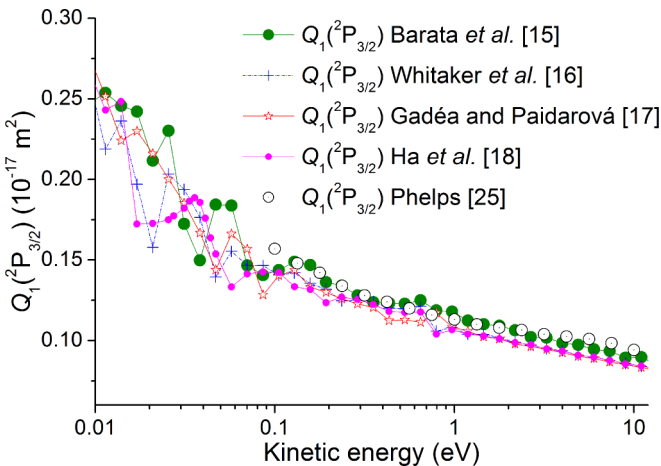


FIG. 9. (Color online) Symmetrized momentum transfer collision cross sections obtained from the several interaction potential curves [15–18] with the inclusion of the spin-orbit interaction as function of kinetic energy for the ions in the ground state $^2P_{3/2}$.

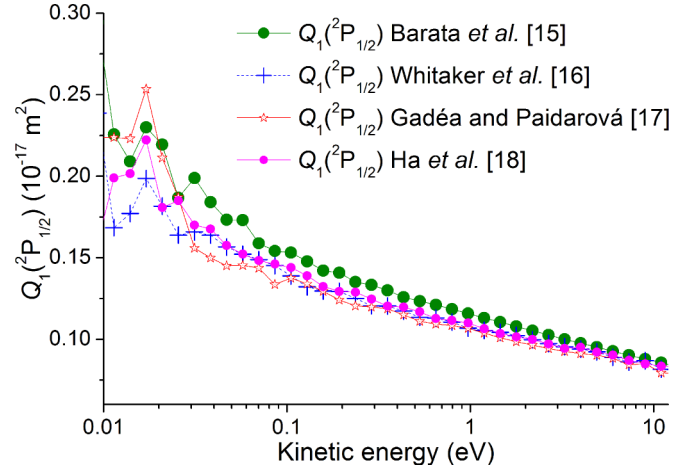


FIG. 10. (Color online) Symmetrized momentum transfer collision cross sections obtained from the several interaction potential curves [15–18] with the inclusion of the spin-orbit interaction as function of the kinetic energy of the ions for the excited state $^2P_{1/2}$.

calculated obtained from the potentials given by Whitaker *et al.* [16] and Ha *et al.* [18] will be similar to each other at all electric fields, the ones calculated from Gad ea and Paidarova’s potentials [17] will be a little larger, and those of Barata *et al.* [15] will be a bit smaller. Moreover, it is noteworthy that the ground and excited state momentum transfer collision cross sections are similar to each other, which is especially true for the integral collision cross sections. Inspection of the cross section opacity shows that the large impact parameters, i.e., the long range part of the potentials, contribute predominantly to the collision cross sections. Since the long range parts of all the potentials are similar (the ion-atom polarization term dominates here), this leads to close collision cross sections and will lead to comparable transport coefficients for the ground $^2P_{3/2}$ and metastable $^2P_{1/2}$ states.

IV. ION TRANSPORT COEFFICIENTS

A. Monte Carlo method

The Monte Carlo algorithm has been used to simulate the transport of Ar^+ ions, in the ground $^2P_{3/2}$ and metastable $^2P_{1/2}$ states, in argon gas under the action of a uniform electric field E (applied along the z axis). Simulation techniques using the Monte Carlo method for transport coefficient calculations have been already detailed elsewhere [9,26]. In short, Monte Carlo code treats an initially great number of seed particles one by one until their disappearance, while elastic and inelastic collisions are defined by their collision cross sections. In addition, fictitious ionization (ion creation) is also considered in order to obtain more accurate results if there are frequent processes of ion removal. The usual approximation of a weakly ionized gas is made, where only interactions between ion and neutral species in their ground states are taken into account. This means that probability of collisions between ion and excited neutral species is assumed negligible. The target gas motion at ambient temperature (300 K) has been taken into account in the calculation of the relative ion energy by considering both ion and target gas velocities. Ion

energy is calculated from the classical dynamics equations by considering the electric field acceleration and the energy of the target gas is determined by assuming a Maxwellian distribution at 300 K.

Transport coefficient data are calculated from Monte Carlo simulation using either the differential collision cross sections without any additional assumption on ion scattering, or using momentum transfer collision cross sections by assuming an isotropic scattering for the calculation of the deviation angle after every collision. In the first case, the deviation angle θ is calculated from the following relation:

$$r_\theta = \frac{\int_0^\theta \sigma_{\text{sym}}(\varepsilon, \theta') \sin(\theta') d\theta'}{\int_0^\pi \sigma_{\text{sym}}(\varepsilon, \theta') \sin(\theta') d\theta'}, \quad (4.1)$$

where r_θ is a random number uniformly distributed in the interval $[0,1]$. In the Ar^+/Ar system, there are not simple analytical expressions for the differential cross section variation as a function of the derivation angle θ (cf. Fig. 5). This means that the unknown deviation angle θ has to be calculated from the numerical solution of Eq. (4.1), which is required for every collision during the Monte Carlo simulation of the ion transport. In fact, such a numerical approach leads to a huge computation time since several millions of collisions have to be considered during the Monte Carlo simulation. To reduce the computation time, the momentum collision cross section can be considered instead as an approximation to indirectly take into account the anisotropy of collisions without using the differential cross section. In this case, the deviation angle is determined by the following relation:

$$\cos(\theta) = 1 - 2r_\theta. \quad (4.2)$$

A simulation using the differential collision cross sections [i.e., the deviation angle calculated from Eq. (4.1)] leads to computation times more than 100 times longer in comparison to the isotropic scattering case [i.e., deviation angle calculated from Eq. (4.2)]. A comparative analysis between reduced mobilities calculated from the differential collision cross section on the one hand and from the momentum collision cross sections on the other hand will be outlined below in Sec. IV B. The description of the successive steps of Monte Carlo algorithms (calculation of the free time of flight, trajectory between collisions, the type of collision, velocities before and after every collision, and transport coefficients) can be found in detail elsewhere [9,26]. Transport coefficients such as reduced mobility K_0 and longitudinal D_L or transversal D_T diffusion coefficients are determined respectively from the following relations:

$$K_0 N = \frac{\langle v_z \rangle}{E/N} \frac{T_0}{T_{\text{gas}}} \frac{P_{\text{gas}}}{P_0}, \quad (4.3)$$

$$D_L = \frac{1}{2} \frac{d[z(t) - \langle z(t) \rangle]^2}{dt}, \quad (4.4)$$

$$D_T = \frac{1}{4} \frac{d\{[x(t) - \langle x(t) \rangle]^2 + [y(t) - \langle y(t) \rangle]^2\}}{dt}, \quad (4.5)$$

where $T_0 = 273.16$ K is the standard temperature, T_{gas} is the gas temperature, $P_0 = 760$ torr is the standard atmospheric pressure, and P_{gas} is the gas pressure. The ion trajectories $x(t)$, $y(t)$, $z(t)$ between two successive collisions are determined

from classical equations where the electric field \vec{E} is applied along the z axis accelerating uniformly the ions during their free flight. Considering the position (or drift velocity) $X_{i,j}$ related to the positive ion number i undergoing collision number j during its drift towards the cathode under the action of the uniform electric field \vec{E} , the mean quantity X is calculated by using a statistical mean from the conventional formula,

$$\langle X \rangle = \frac{1}{n_p} \sum_{i=1}^{n_p} \frac{1}{n_c} \sum_{j=1}^{n_c} X_{i,j}, \quad (4.6)$$

where n_p is the number of seed particles and n_c is the total number of collisions occurring during the whole ion pathway from its emission at the anode to its disappearance at the cathode (or during non-conservative inelastic collision processes). Such a definition is consistent with the uniform electric field condition and steady state regime reached in the case of standard drift tubes used for ion mobility measurements [27].

B. Results and discussion

The number of seed particles n_p considered in the Monte Carlo simulation was taken as $n_p = 5\,000\,000$ for $E/N \leq 10$ Td, $n_p = 1\,000\,000$ for $10 < E/N \leq 100$ Td and $n_p = 100\,000$ for higher electric fields, in order to use the Monte Carlo method as a reliable tool for the precision estimate of the different interaction potentials. These numbers of seed particles, which give negligible statistical errors on calculated transport coefficients, were determined from a previous detailed study [4]. The seed particles are considered in the simulation until their disappearance either when an inelastic process occurs (for instance, spin change processes lead to the disappearance of the considered $^2P_{3/2}$ or $^2P_{1/2}$ ion) or when the maximum simulation time is elapsed. Convergence parameters, namely ε_{max} (the maximum energy required for a given E/N) and the maximum time t_{max} (chosen longer than the ion relaxation time for every E/N), vary respectively from 0.7 to 12 eV and from 0.4 to 1 μs for reduced electric fields varying between 1 and 1500 Td. The ion energy distribution functions given by the Monte Carlo simulation show that, for ions in the ground state $^2P_{3/2}$, the ion energy does not exceed $\varepsilon = 0.3$ eV at 1 Td, $\varepsilon = 4$ eV at 500 Td, and $\varepsilon = 12$ eV at 1500 Td (cf. Fig. 11). This also remains valid for ions in the excited state $^2P_{1/2}$ since the corresponding ion distribution function is similar to that obtained for ions in the $^2P_{3/2}$ state. This can be easily understood since the corresponding collision cross sections $Q_1(^2P_{3/2})$ and $Q_1(^2P_{1/2})$ are quite close to each other.

As a first step, the reduced ion mobility data $K_0(^2P_{3/2})$ of the ground state ($^2P_{3/2}$) Ar^+ ion in Ar have been calculated using the $^2P_{3/2}$ differential collision cross sections obtained for the different interaction potentials considered in Sec. II [15–18]. The spin change transition ($3/2, 1/2 \rightarrow 1/2, 1/2$) is considered as an inelastic process which leads to the disappearance of $\text{Ar}^+(^2P_{3/2})$ ions. The E/N dependence of the calculated $^2P_{3/2}$ reduced mobility data calculated for the different interaction potentials is shown in Fig. 12 and listed in Table III. The experimental mobility data of Helm

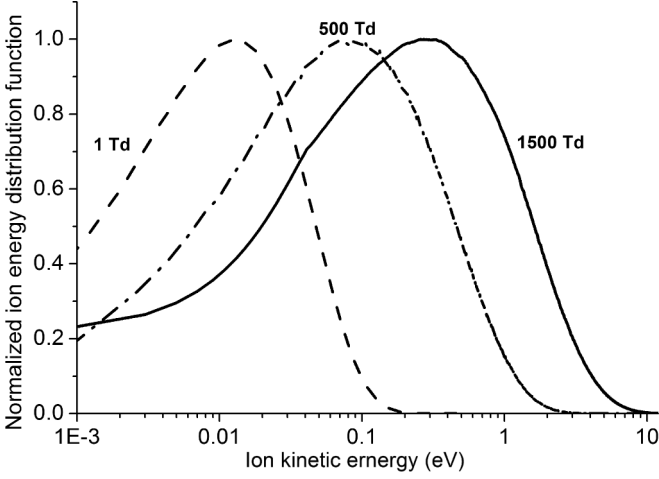


FIG. 11. Normalized energy distribution function of ${}^2P_{3/2}$ ions for reduced fields $E/N = 1, 500,$ and 1500 Td.

and Elford [11], Hegerberg *et al.* [12], Basurto *et al.* [14], and those compiled by Ellis *et al.* [13] (from Beatty [28] and Hornbeck [29]) are also shown in Fig. 12 for comparison with an experimental error of 1% for $E/N < 250$ Td and 3% for higher electric fields. For the reader's convenience, the experimental mobility data are listed in Table IV. It is clear from Fig. 12 that the mobilities calculated by using Gadéa and Páidarová's [17] and Whitaker *et al.*'s [16] potentials show a good agreement with Ellis *et al.* [13], Helm and Elford [11], and Hegerberg [12] experimental results.

To illustrate the performance of the interaction potentials, the relative and standard errors with respect to the experimental data of Ellis *et al.* [13], Basurto *et al.* [14], and the association of the data by Helm and Elford [11] and Hegerberg [12] have been calculated. Mobility data calculated by using Gadéa and Páidarová's interaction potential curves [17] give the best agreement where standard errors of $SE = 0.0060 \text{ cm}^2 \text{ V}^{-1} \text{ s}^{-1}$ and $SE = 0.0007 \text{ cm}^2 \text{ V}^{-1} \text{ s}^{-1}$ were obtained, respectively, from Ellis *et al.* [13] data and the association of Helm and

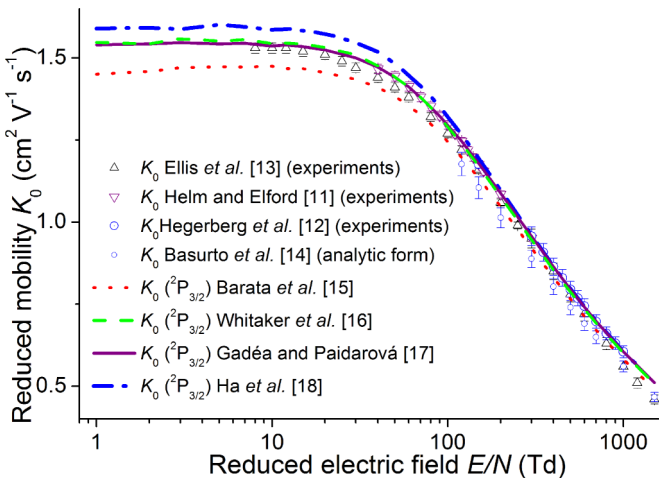


FIG. 12. (Color online) Comparison between measured ion mobility [11–14] and calculated ones for ions in the ground state ${}^2P_{3/2}$ using interaction potentials [15–18].

TABLE III. Calculated reduced mobilities in $\text{cm}^2 \text{ V}^{-1} \text{ s}^{-1}$ of Ar^+ ions in the ground state ${}^2P_{3/2}$ in Ar from several interaction potentials [15–18] and the associated standard errors (SE) with respect to experimental data [11–14].

E/N (Td)	References of potentials			
	Barata <i>et al.</i> [15]	Whitaker <i>et al.</i> [16]	Gadéa and Páidarová [17]	Ha <i>et al.</i> [18]
1	1.45	1.55	1.54	1.59
2	1.46	1.54	1.54	1.59
3	1.47	1.56	1.55	1.59
5	1.47	1.55	1.54	1.60
7	1.47	1.56	1.54	1.59
10	1.47	1.54	1.54	1.59
12	1.47	1.55	1.54	1.59
15	1.47	1.54	1.53	1.58
20	1.45	1.53	1.52	1.57
30	1.43	1.51	1.50	1.55
40	1.41	1.48	1.47	1.52
50	1.38	1.44	1.44	1.48
60	1.35	1.41	1.41	1.45
70	1.33	1.38	1.38	1.41
80	1.30	1.35	1.35	1.38
90	1.27	1.32	1.32	1.35
100	1.24	1.29	1.29	1.32
120	1.20	1.24	1.25	1.27
150	1.13	1.17	1.18	1.19
200	1.05	1.08	1.09	1.10
300	0.92	0.95	0.96	0.96
400	0.83	0.85	0.86	0.87
500	0.77	0.79	0.79	0.79
600	0.71	0.73	0.74	0.75
700	0.67	0.69	0.70	0.70
1000	0.58	0.60	0.60	0.61
1500	0.49	0.51	0.51	0.51
SE Ellis <i>et al.</i> [13]	0.0078	0.0060	0.0060	0.0122
SE Helm and Hegerberg [11,12]	0.0113	0.0016	0.0007	0.0062
SE Basurto <i>et al.</i> [14]	0.0083	0.0166	0.0190	0.0211

Hegerberg [11,12] data. The maximum relative deviation is 11.1% at 1500 Td from Ellis *et al.* data and 0.63% at 300 Td from Helm and Hegerberg data. Results obtained by using Whitaker *et al.*'s interaction potential curves [16] show also excellent agreement experimental data. A standard error of $SE = 0.0060 \text{ cm}^2 \text{ V}^{-1} \text{ s}^{-1}$ and a maximal relative deviation of 10.5% at 1500 Td were obtained from experimental data of Ellis *et al.* [13], while a standard error of $SE = 0.0016 \text{ cm}^2 \text{ V}^{-1} \text{ s}^{-1}$ and a maximal relative deviation of 1.21% at 600 Td were obtained from Helm and Hegerberg measurements [11,12]. However, Ha *et al.*'s [18] and Barata *et al.*'s [15] potential curves lead to higher standard errors respectively equal to $SE = 0.0122 \text{ cm}^2 \text{ V}^{-1} \text{ s}^{-1}$ and $SE = 0.0078 \text{ cm}^2 \text{ V}^{-1} \text{ s}^{-1}$ from Ellis *et al.* [13] data and $SE = 0.0062 \text{ cm}^2 \text{ V}^{-1} \text{ s}^{-1}$ and $SE = 0.0113 \text{ cm}^2 \text{ V}^{-1} \text{ s}^{-1}$ from the association of Helm and Hegerberg [11,12] data. The standard errors obtained from Basurto *et al.*'s measurements [14] are much higher for the

TABLE IV. Measured reduced mobilities in $\text{cm}^2 \text{V}^{-1} \text{s}^{-1}$ of Ar^+ ions in Ar.

E/N (Td)	References			
	Helm and Elford [11]	Hegerberg <i>et al.</i> [12]	Ellis <i>et al.</i> [13]	Basurto <i>et al.</i> [14]
8			1.53	
10			1.53	
12			1.53	
15			1.52	
20			1.51	
30			1.47	
40	1.47		1.44	
50	1.44		1.41	
60	1.41		1.38	
70	1.38			
80	1.35		1.32	
90	1.32			
100	1.30		1.27	
120	1.25		1.22	1.18
150	1.18	1.18	1.16	1.10
200	1.09		1.06	1.01
300	0.95		0.95	0.89
400		0.86	0.85	0.80
500		0.80	0.78	0.74
600		0.74	0.72	0.69
700		0.70		0.65
1000		0.61	0.56	0.56
1500			0.46	0.47

interaction potentials of Gadéa and Paidarová and Whitaker *et al.*, which show the best agreement with other experiments [11–13]. From these first transport coefficients results, it is noteworthy that the mobility data measured by Helm and Elford [11] and Hegerberg *et al.* [12] give the best agreement with the calculated *ab initio* transport coefficients, i.e., when mobilities are calculated by using potentials given by Whitaker *et al.* [16], Gadéa and Paidarová [17], or Ha *et al.* [18]. The relative deviations between our calculations and Helm and Hegerberg experiments [11,12] are summarized in Fig. 13.

These results presented above are valid only if $^2P_{3/2}$ ions are considered in experiments. But, in reality the background weakly ionized gas also contains, in addition to a major proportion of ions in the $^2P_{3/2}$ state, a small proportion of $^2P_{1/2}$ ions (p_{met}). In order to confirm the excellent agreements of the mobilities calculated by using Gadéa and Paidarová’s [17] or Whitaker’s [16] interaction potentials with the experimental results of Helm and Hegerberg [11,12], standard errors have to be calculated for linearly weighted averages of the mobilities obtained for both ionic states:

$$K_0 = (1 - p_{\text{met}})K_0(^2P_{3/2}) + p_{\text{met}}K_0(^2P_{1/2}), \quad (4.7)$$

with different proportions of metastable ions (p_{met}). Then, as a second step, the reduced ion mobility data $K_0(^2P_{1/2})$ of Ar^+ ion in $^2P_{1/2}$ state have been calculated using the $^2P_{1/2}$ differential collision cross sections obtained for the different interaction potentials [15–18] (cf. Sec. II). The mobilities are shown in Fig. 14 and listed in Table V. Experimental data are shown as

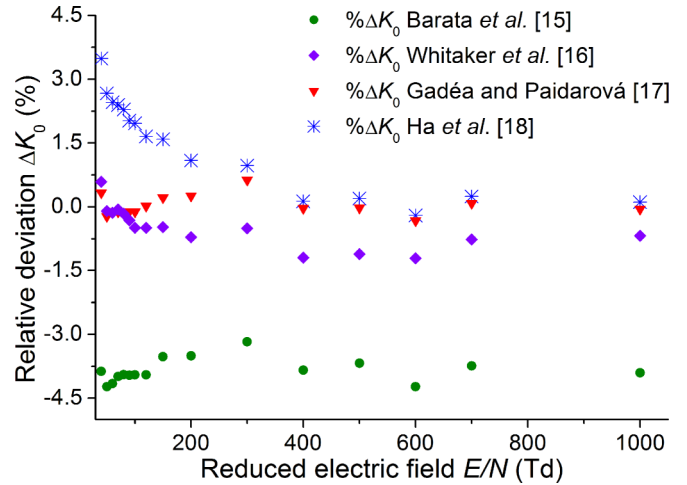


FIG. 13. (Color online) Relative deviation between reduced mobility obtained from the association of Helm and Elford [11] and Hegerberg *et al.* [12] experimental results and from collision cross sections calculated using the interaction potentials [15–18].

a reference only. It is noteworthy that for each potential, the mobilities obtained for ions in the metastable state $^2P_{1/2}$ are as expected close to the ones obtained for ions in the ground state $^2P_{3/2}$ (cf. Figs. 12 and 14).

This confirms the observations done by Helm and Elford [11] who could not measure separately mobilities of ions in the ground state and in the metastable state and, thus, concluded that the mobilities of Ar^+ ions in either states lay within $\pm 1\% - 5\%$.

The $^2P_{3/2}$ and $^2P_{1/2}$ ion mobilities have then been mixed as shown in Eq. (4.7) for each of the considered interaction potentials and the corresponding standard errors were calculated with respect to the experimental results [11–14] for a proportion of metastable ions ranging between 0.02 and 0.2. Standard errors calculated for the various proportions of metastable ions with respect to Ellis *et al.*’s [13] mobility data show that the use of Gadéa and Paidarová’s [17] or

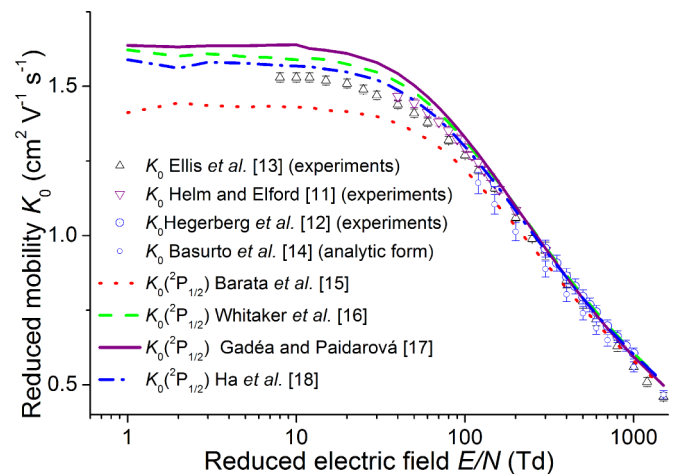


FIG. 14. (Color online) Calculated ion mobility data for ions in the metastable state $^2P_{1/2}$ using interaction potentials [15–18]. Experimental data [11–14] are also shown for reference.

TABLE V. Calculated reduced mobilities in $\text{cm}^2 \text{V}^{-1} \text{s}^{-1}$ of Ar^+ ions in the excited state $^2P_{1/2}$ in Ar from several interaction potentials [15–18].

E/N (Td)	References of potentials			
	Barata <i>et al.</i> [15]	Whitaker <i>et al.</i> [16]	Gadéa and Páidarová [17]	Ha <i>et al.</i> [18]
1	1.41	1.62	1.64	1.59
2	1.44	1.60	1.63	1.56
3	1.44	1.61	1.64	1.58
5	1.43	1.60	1.64	1.58
7	1.43	1.60	1.64	1.57
10	1.43	1.59	1.64	1.57
12	1.43	1.59	1.63	1.57
15	1.42	1.59	1.62	1.56
20	1.42	1.57	1.61	1.55
30	1.40	1.55	1.58	1.52
40	1.38	1.52	1.54	1.49
50	1.35	1.48	1.50	1.45
60	1.32	1.45	1.47	1.42
70	1.30	1.41	1.43	1.39
80	1.27	1.38	1.39	1.36
90	1.25	1.35	1.36	1.33
100	1.22	1.32	1.33	1.30
120	1.17	1.26	1.27	1.25
150	1.11	1.20	1.20	1.18
200	1.03	1.10	1.10	1.08
300	0.91	0.96	0.96	0.95
400	0.82	0.87	0.86	0.86
500	0.76	0.80	0.79	0.79
600	0.71	0.74	0.73	0.74
700	0.67	0.70	0.69	0.69
1000	0.58	0.60	0.59	0.60
1500	0.49	0.51	0.50	0.51

Whitaker *et al.*'s [16] interaction potential curves leads to the best agreement with similar SE varying between about 0.0062 and 0.0077 $\text{cm}^2 \text{V}^{-1} \text{s}^{-1}$. However, standard errors with respect to Basurto *et al.*'s [14] data show that potentials by Barata *et al.* [15] give the best agreement with a minimal $\text{SE} = 0.0077 \text{ cm}^2 \text{V}^{-1} \text{s}^{-1}$ for $p_{\text{met}} = 0.2$. However, this result is not consistent since the agreement improves with increasing the metastable proportion p_{met} . Moreover, the interaction potential of Barata *et al.* is not an *ab initio* potential but an analytical fit adjusted from experimental spectroscopy data. The standard errors calculated with respect to the association of the Helm and Hegerberg measurements [11,12] confirm the previous observations. Indeed, the best agreement is found for the potentials of Gadéa and Páidarová [17] and Whitaker *et al.* [16] with standard errors SE varying between 0.0007 and 0.0019 $\text{cm}^2 \text{V}^{-1} \text{s}^{-1}$. The lowest standard mobility errors SE are obtained with respect to Helm and Hegerberg measurements when Gadéa and Páidarová's or Whitaker *et al.*'s potentials are used for the calculation of collision cross sections. Figure 15 displays the standard errors obtained for the considered interaction potentials [15–18] with respect to Helm and Hegerberg measurements for different p_{met} proportions. It is noteworthy that the proportion of metastable ions does not influence considerably the mobility results except for Gadéa

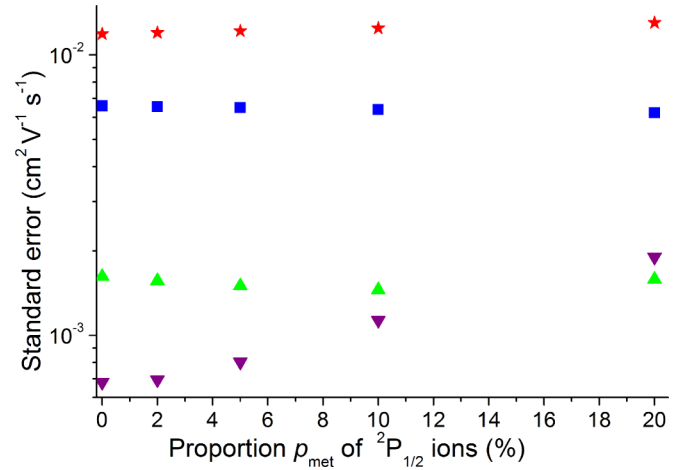


FIG. 15. (Color online) Standard errors of the mobility obtained for Barata *et al.* (\star), Whitaker *et al.* (\blacktriangle), Gadéa and Páidarová (\blacktriangledown), and Ha *et al.* (\blacksquare) for different proportions of ions in the metastable state from the association of Helm and Elford [11] and Hegerberg *et al.* [12] experimental results.

and Páidarová for which the standard deviation SE increases with the p_{met} proportion. From these results, it is clear that the proportion of metastable ions is highly probably small (0–5%) in the experiment, in agreement with experimental conclusions [11].

In addition to the ion mobility, other ion transport coefficients such as longitudinal and transversal diffusion characteristic energies, respectively, eD_L/K and eD_T/K ($K = K_0N$), which are needed for multidimensional modeling of plasma jet electrodynamics, were also calculated using the interaction potential curves by Gadéa and Páidarová. Figure 16 shows the calculated characteristic energies plotted against the reduced electric field for the $^2P_{3/2}$ ion. The obtained transversal coefficients are within the $\pm 5\%$ error bars of

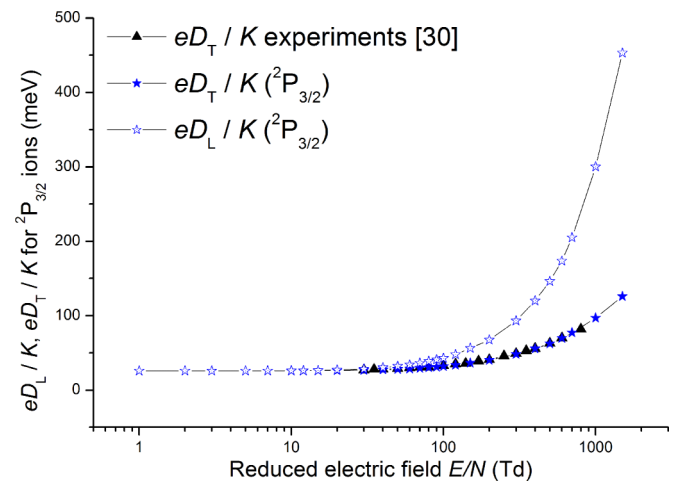


FIG. 16. (Color online) Transversal eD_T/K and longitudinal eD_L/K diffusion characteristic energies for Ar^+ ions in the ground state calculated using the interaction potential curves of Gadéa and Páidarová [17]. The experimental results [30] of eD_T/K are shown for comparison.

TABLE VI. Calculated transversal eD_T/K and longitudinal eD_L/K diffusion characteristic energies in meV for Ar^+ ions $^2P_{3/2}$ and $^2P_{1/2}$ states using Gadéa and Paidarová's [17] interaction potential curves.

E/N (Td)	$^2P_{3/2}$		$^2P_{1/2}$	
	eD_T/K	eD_L/K	eD_T/K	eD_L/K
1	25.93	25.99	25.73	25.701
2	25.91	25.90	25.68	25.63
3	25.83	25.85	25.92	25.98
5	25.93	25.95	25.93	26.01
7	25.86	26.02	25.85	25.99
10	25.99	26.15	25.90	26.15
12	25.95	26.27	26.14	26.32
15	26.15	26.47	26.18	26.66
20	26.27	27.20	26.40	27.10
30	26.79	28.47	26.92	28.50
40	27.35	30.25	27.59	30.30
50	28.04	32.15	28.37	32.06
60	28.70	34.10	29.19	34.20
70	29.49	36.29	30.13	36.14
80	30.40	38.72	30.85	38.50
90	31.13	40.90	31.71	40.67
100	32.00	42.89	32.50	43.08
120	33.61	47.78	34.15	48.00
150	36.47	56.40	36.85	55.27
200	40.27	67.50	40.39	67.67
300	48.32	93.21	48.13	94.55
400	55.69	119.97	55.34	121.17
500	62.40	146.21	62.88	149.16
600	69.75	173.62	70.59	179.66
700	77.28	205.16	76.88	208.13
1000	96.98	300.28	98.07	301.45
1500	125.87	453.18	131.75	468.03

transverse diffusion measurements compiled by Viehland and Mason [30]. Diffusion characteristic energies are also listed in Table VI for both $^2P_{3/2}$ and $^2P_{1/2}$ ions. It is clear from Fig. 16 and Table VI that, at low electric field ($E/N = 1$ Td), longitudinal and transversal characteristic energies converge as expected to about a 25.8 meV average. This value is consistent with the one obtained for $T = 300$ K from the Nernst-Townsend-Einstein relation [31], which is valid in weak fields when the diffusion becomes isotropic (i.e., $D_L = D_T = D$),

$$eD/K = k_B T. \tag{4.8}$$

Here k_B is the Boltzmann constant, T is the background gas temperature, and e is the electric charge of the ion.

Our mobility and diffusion coefficients results obtained for $\text{Ar}^+(^2P_{3/2})$ and $\text{Ar}^+(^2P_{1/2})$ ions (cf. Tables III, V, and VI) can be compared to the previous calculation of Viehland and Hesche [32]. In this study they computed the collision cross section using the Michels *et al.*'s [33], Wadt's [34], and Dehmer and Dehmer's [35] Ar_2^+ interaction potentials with the JWKB approximation. Ion transport coefficients are obtained from the kinetic theory based on moments of Boltzmann equation. Whereas our best mobility calculation are less than 1% in error with respect to experimental data

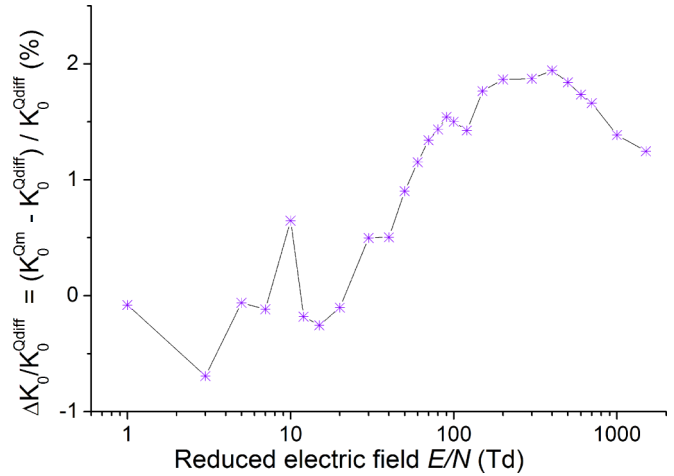


FIG. 17. (Color online) Relative deviation between reduced mobility obtained from the differential collision cross sections and from the momentum transfer ones calculated from the potential curves given by Gadéa and Paidarová [17].

(cf. Fig. 13), their results show only a good qualitative agreement with deviations from experiments that can reach 10%. The present work provides improvement both in the accuracy of the potentials and in the transport coefficients calculated from the collision cross sections.

On the other hand, it has been shown in Sec. III that the spin change ($3/2, 1/2 \rightarrow 1/2, 1/2$) and ($1/2, 1/2 \rightarrow 3/2, 1/2$) collision cross sections are negligible against the other contributions to the $^2P_{3/2}$ and $^2P_{1/2}$ collision cross sections [cf. Eqs. (3.8) and (3.9)]. Additional Monte Carlo calculations ignoring ($3/2, 1/2 \rightarrow 1/2, 1/2$) and ($1/2, 1/2 \rightarrow 3/2, 1/2$) spin change processes lead to similar transport coefficient results.

As a final step, mobilities were calculated using the momentum transfer collision cross sections to confirm the expectation that the resulting mobilities are within a maximal relative deviation of $\pm 2\%$ from the exact results [4]. Relative deviations between Monte Carlo mobilities for ions in the ground state $^2P_{3/2}$ calculated by using the differential collision cross sections obtained from Gadéa and Paidarová's [17] potential curves and the corresponding momentum transfer collision cross sections are displayed for various reduced electric fields (E/N) in Fig. 17. This figure shows that the relative deviation between reduced mobilities calculated using the differential cross section and the momentum cross section does not exceed $\pm 2\%$. This maximum deviation remains valid for all other potentials as well as for the $^2P_{1/2}$ state. Moreover, the use of the momentum transfer collision cross sections rather than the differential ones reduces the computation time by at least of two orders of magnitude.

V. CONCLUSIONS

Collision cross sections have been calculated using a close coupling quantum method from different *ab initio* interaction potentials, with the inclusion of the spin-orbit interaction, for Ar^+ ions, either in the ground $^2P_{3/2}$ state or in the metastable $^2P_{1/2}$ state, colliding with Ar. The corresponding ion transport coefficients have further been calculated using an optimized

Monte Carlo code and compared to available experimental results. The agreement is very good which clearly demonstrates that it is possible to compute *ab initio* transport properties with high accuracy. The best agreement between theory and experiment has been found for the Gadéa and Paidarová's [17] or Whitaker *et al.*'s [16] electronic potential curves. In the two cases, the minimum average relative errors between our calculations and experimental data of Helm and Elford [11] and Hegerberg *et al.* [12] have been found, respectively, less than 0.2% and 0.6%, which can presumably be considered as the most accurate experimental results. This may presumably lead us to a conclusion that the two sets of experimental data may be considered as the most accurate. The transversal and longitudinal diffusion coefficients have been obtained from the Gadéa and Paidarová's and Whitaker *et al.*'s interaction potential curves within the error bars of available experimental results. Therefore, the interaction potential curves of Gadéa

and Paidarová's or Whitaker *et al.*'s will be used in the diatomic-in-molecules (DIM) model, in a forthcoming work, to study the Ar_2^+/Ar interaction system and to obtain the corresponding ion transport data. Moreover, it has been shown that the spin change processes do not have a significant influence on the ion transport coefficients obtained both for the ground state ions ($^2P_{3/2}$) and metastable ions ($^2P_{1/2}$). Ion transport coefficients have also been calculated from an approximate approach using the momentum transfer collision cross sections. It has been shown that this approximation leads to mobility results with a maximal deviation of $\pm 2\%$ from the exact ones, in agreement with a previous study [4]. However, a gain of a factor larger than 100 in computing time has been observed in the former case. Therefore, the approach based on the momentum transfer cross sections can be considered as an interesting approximation for further studies.

-
- [1] M. G. Kong, G. Kroesen, G. Morfill, T. Nosenko, T. Shimizu, J. Van Dijk, and J. L. Zimmermann, *New J. Phys.* **11**, 115012 (2009).
- [2] M. Yousfi, N. Merbahi, A. Pathak, and O. Eichwald, *Fundamental Clinical Pharmacol.* **28**, 123 (2014).
- [3] M. Yousfi, O. Eichwald, N. Merbahi, and N. Jomaa, *Plasma Sources Sci. Technol.* **21**, 045003 (2012).
- [4] A. Chicheportiche, B. Lepetit, M. Benhenni, F. X. Gadéa, and M. Yousfi, *J. Phys. B* **46**, 065201 (2013).
- [5] A. Chicheportiche, M. Benhenni, M. Yousfi, B. Lepetit, R. Kalus, and F. X. Gadéa, *Phys. Rev. E* **88**, 043104 (2013).
- [6] J. L. Walsh and M. G. Kong, *Appl. Phys. Lett.* **91**, 221502 (2007).
- [7] S. J. Kim, T. H. Chung, and S. H. Bae, *Phys. Plasmas* **17**, 053504 (2010).
- [8] W. V. Gaens and A. Bogaerts, *J. Phys. D* **46**, 275201 (2013).
- [9] M. Yousfi, A. Hennad, and A. Alkaa, *Phys. Rev. E* **49**, 3264 (1994).
- [10] J. S. Cohen and B. Schneider, *J. Chem. Phys.* **61**, 3230 (1974).
- [11] H. Helm and M. T. Elford, *J. Phys. B* **10**, 3849 (1977).
- [12] R. Hegerberg, M. T. Elford, and H. R. Skullerud, *J. Phys. B* **15**, 797 (1982).
- [13] H. W. Ellis, R. Y. Pai, E. W. McDaniel, E. A. Mason, and L. A. Viehland, *At. Data Nucl. Data Tables* **17**, 177 (1976).
- [14] E. Basurto, J. de Urquijo, I. Alvarez, and C. Cisneros, *Phys. Rev. E* **61**, 3053 (2000).
- [15] J. Barata, *Nucl. Instrum. Methods Phys. Res. A* **580**, 14 (2007).
- [16] B. J. Whitaker, C. A. Woodward, P. J. Knowles, and A. J. Stace, *J. Chem. Phys.* **93**, 376 (1990).
- [17] F. X. Gadéa and I. Paidarová, *Chem. Phys.* **209**, 281 (1996).
- [18] T. K. Ha, P. Rupper, A. Wüest, and F. Merkt, *Mol. Phys.* **101**, 827 (2003).
- [19] M. Child, *Molecular Collision Theory* (Dover, Mineola, NY, 1996).
- [20] T. Wu and T. Ohmura, *Quantum Theory of Scattering* (Prentice-Hall, Englewood Cliffs, NJ, 1962).
- [21] A. Kramida, Yu. Ralchenko, J. Reader, and NIST ASD Team (2013), *At. Spectra Database* (ver. 5.1), <http://physics.nist.gov/asd>
- [22] A. Wüest and F. Merkt, *J. Chem. Phys.* **120**, 638 (2004).
- [23] R. De Vogelaere, *J. Res. Natl. Bur. Stand.* **54**, 119 (1955).
- [24] R. B. Bernstein, *Atom-Molecule Collision Theory: A Guide for the Experimentalist* (Plenum, New York, 1979).
- [25] A. V. Phelps, *J. Phys. Chem. Data* **20**, 557 (1991).
- [26] M. Yousfi, A. Hennad, and O. Eichwald, *J. Appl. Phys.* **84**, 107 (1998).
- [27] M. Benhenni, J. de Urquijo, M. Yousfi, J. L. Hernandez-Ávila, N. Merbahi, G. Hinojosa, and O. Eichwald, *Phys. Rev. E* **71**, 036405 (2005).
- [28] E. C. Beaty, Proc. Fifth Int. Conf. on Ionization Phenomena Gases, Munich, 183 (1961).
- [29] J. A. Hornbeck, *Phys. Rev.* **84**, 615 (1951).
- [30] L. A. Viehland and E. A. Mason, *At. Data Nucl. Data Tables* **60**, 37 (1995).
- [31] P. Watts and A. Wilders, *Int. J. Mass Spectrom. Ion Processes* **112**, 179 (1992).
- [32] L. A. Viehland and M. Hesche, *Chem. Phys.* **110**, 41 (1986).
- [33] H. H. Michels, R. H. Hobbs, and L. A. Wright, *J. Chem. Phys.* **69**, 5151 (1978).
- [34] W. R. Wadt, *J. Chem. Phys.* **68**, 402 (1978).
- [35] P. M. Dehmer and J. L. Dehmer, *J. Chem. Phys.* **69**, 125 (1978).